Catalysis
Science &
Technology

ROYAL SOCIETY
OF CHEMISTRY

PAPER

View Article Online
View Journal

Check for updates

Cite this: DOI: 10.1039/d1cy00273b

Oxidation of methane to methanol over Pd@Pt nanoparticles under mild conditions in water†

Jianjun Chen,‡[ab] Sikai Wang,‡[ac] Laurent Peres,[d] Vincent Collière,[d] Karine Philippot,[d] Pierre Lecante,[e] Yaoqiang Chen*[b] and Ning Yan*[a]

Received 12th February 2021,
Accepted 19th March 2021

DOI: 10.1039/d1cy00273b

rsc.li/catalysis

Direct methane oxidation into oxygen-containing chemicals under mild conditions has sparked increasing interest. Here, we report Pd@Pt core–shell nanoparticles that efficiently catalyse the direct oxidation of CH_4 to CH_3OH in water using H_2O_2 as an oxidant under mild conditions. The catalyst presents a methanol productivity of up to 89.3 mol $kg_{catalyst}^{-1}$ h^{-1} with a high selectivity of 92.4% after 30 min at 50 °C, thus outperforming most of the previously reported catalysts. Electron-enriched Pt species in the Pd@Pt nanoparticles were identified by structural and electronic analysis. Pd in the core donates electrons to Pt, leading to higher rates of methane activation. Based on the results of control experiments and kinetic analysis, a consecutive oxidation pathway *via* a radical mechanism is proposed, which includes initial formation of CH_3OOH and CH_3OH followed by further oxidation of CH_3OH to HCHO, HCOOH, and CO_2.

1. Introduction

Natural gas is receiving great attention as a valuable source of energy and chemicals.[1,2] As the main component of natural gas, methane is extensively applied as a fuel and also processed into chemicals.[3–5] To date, large-scale conversion of methane to liquid hydrocarbons in industry has been carried out through indirect methane-steam reforming coupled with Fischer–Tropsch synthesis.[6–10] These steps normally involve harsh conditions with high temperature (>400 °C) and pressure (>10 bar).[11–15] Direct conversion of methane into value-added liquid fuels and chemicals such as methanol, olefins, hydrogen, and aromatics has thus become an important research topic attracting interest from both industry and academia.[16–18]

The direct conversion pathways include methane pyrolysis,[19] oxidative coupling,[20,21] and partial oxidation.[22,23] Among these, oxidation pathways are exothermic and low-temperature favoured. For instance, direct oxidation of methane into methanol ($CH_4 + 0.5\ O_2 \rightarrow 3CH_3OH$) has a ΔH^0_{298K} value of −126.4 kJ mol^{-1}. Over a range of oxidants, such as O_2, H_2O_2, and N_2O, partial oxidation has been proven viable below 200 °C. Compared to the indirect syngas process, it is simpler and potentially more effective, but there are two main issues to overcome. First, the C–H bond in methane is difficult to activate due to the high ionization energy, high bond energy, low polarity, and low electron and proton affinity of methane.[24–26] Second, it is thermodynamically difficult to keep the formed methanol because the dissociation energy of the C–H bond in methanol (392 kJ mol^{-1}) is lower than that in methane (439 kJ mol^{-1}). Under typical reaction conditions, methanol is thus easily oxidized to CO_2.[6,27–29]

Results from decades of research showed that certain homogeneous and heterogeneous catalysts are active for the selective oxidation of methane into C1 oxygenates at low temperatures.[30] For instance, molecular complexes of Pd, Rh, Au, Hg, Ru, and Pt directly oxidized methane into methanol,[26,31,32] but toxic/corrosive reagents such as hydrobromic acid, trifluoroacetic acid, oleum, or hydrochloric acid were heavily used. In heterogeneous catalysis, zeolite-stabilized Fe and Cu species are known to convert CH_4 into methanol *via* stepwise, separated reaction steps.[33–40] In a single-step manner,[41–47] a few systems have been identified to be effective as well. For instance, iron atoms confined in graphene showed high selectivity (94%) to C1 products (CH_3OOH, CH_3OH, $HOCH_2OOH$ and HCOOH) at 25 °C using H_2O_2 as an oxidant.[48] TiO_2 nanoparticle

---

[a] *Department of Chemical and Biomolecular Engineering, National University of Singapore, 4 Engineering Drive, Singapore 117585, Singapore. E-mail: ning.yan@nus.edu.sg*

[b] *Institute of New Energy and Low-carbon Technology, Sichuan University, Chengdu 610064, China. E-mail: chenyaoqiang@scu.edu.cn*

[c] *Joint School of National University of Singapore and Tianjin University, International Campus of Tianjin University, Binhai New City, Fuzhou 350207, China*

[d] *CNRS, LCC (Laboratoire de Chimie de Coordination), 205 route de Narbonne, BP44099, F-31077 Toulouse Cedex 4, France*

[e] *CNRS, CEMES (Centre d'Élaboration des Matériaux et d'Études Structurales), 29 Rue Jeanne-Marvig, BP 4347, F-31055 Toulouse Cedex 4, France*

† Electronic supplementary information (ESI) available. See DOI: 10.1039/d1cy00273b

‡ These authors contributed equally to this work.

supported Cr catalysts achieved similar selectivity at 50 °C.[49] Concerning noble metal-containing catalysts, much progress has been achieved with Au–Pd colloid-based catalysts.[50–52] Hutchings *et al.*[53] reported high selectivity (92%) and methanol productivity (53.6 mol kg_{AuPd}^{-1} h^{-1}) over Au–Pd nanoparticles using H_2O_2 as an oxidant. Very recently, Xiao *et al.*[54] prepared hydrophobic ZSM-5 as a molecular fence for *in situ* H_2O_2 generation that led to the selective oxidation of methane to methanol. This fence permitted the diffusion of hydrophobic species like methane, oxygen, and hydrogen to PdAu active sites over the colloidal catalyst, while locally concentrating the formed H_2O_2 that allowed its rapid interaction with methane.

Besides Au, heterogeneous noble metal catalysts for oxidizing methane to methanol and other oxygenates are currently not common. The CH_3 intermediate is a key precursor for methanol formation in direct oxidation of methane.[22,41,55] Based on DFT calculation, platinum clusters with high proportion of highly coordinatively unsaturated sites are predicted to effectively stabilize the CH_3 intermediate by hindering its successive dehydrogenation.[56–58] The design of Pt-based colloids by incorporating a second metal to change their geometric and electronic structures may be a viable approach to identify suitable catalysts to convert methane to C1 oxygenates.

Motivated by these analyses, in this work, a core–shell Pd@Pt catalyst dispersed in water was developed. Its structural characteristics were investigated by TEM, WAXS, CO-DRIFTS, and XPS. This catalyst was evaluated in the direct oxidation of CH_4 to CH_3OH using H_2O_2 as an oxidant under mild reaction conditions. The catalytic performance was correlated to the structure of the Pd@Pt core–shell nanoparticles, while the reaction pathway was established on the basis of control experiments and reaction kinetic analysis.

2. Experimental methods

2.1 Catalyst synthesis

Monometallic Pt, monometallic Pd, and bimetallic Pt_xPd_y nanoparticles (NPs) were synthesized by a wet chemistry method using water as a solvent to provide the colloidal catalyst. The studied x/y ratios were 8/1, 4/1, 2/1, 1/1, 1/2, 1/4 and 1/8, respectively. Typically, the procedure for the preparation of the Pt_1Pd_1 colloid was as follows: an acidic solution of the $PdCl_2$ precursor and an aqueous solution of the K_2PtCl_4 precursor were dissolved in de-ionized water (500 mL) at a total metal concentration of 0.256 mmol L^{-1}. Polyvinylpyrrolidone (PVP; MW 40 000) was used as a stabilizer and added to the solution at a metal-to-PVP ratio of 1 : 1.2. After vigorously stirring for 30 min, a freshly prepared $NaBH_4$ (0.1 M) aqueous solution was slowly added to the metal precursor/PVP mixture at room temperature (r.t.) and at a metal-to-$NaBH_4$ ratio of 1 : 5. The colour of the solution immediately turned dark. The stirring was maintained for 1 h. For the core–shell systems, namely Pd@Pt NPs and Pt@Pd NPs, Pd (or Pt) NPs were firstly prepared by $NaBH_4$ reduction of the same metal precursors at r.t. Then the Pt (or Pd) precursor was reduced in a second step at a lower temperature (~0 °C). The second step was conducted at a lower temperature to slow down the reduction of the second metal precursor, to favor its reduction at the surface of pre-formed NPs.

2.2 Catalytic performance testing and product analysis

The catalytic performance testing for direct methane oxidation was performed in a stainless-steel autoclave reactor (30 mL). The reactor was charged with a H_2O_2 aqueous solution (400 μmol, 1 M, 0.4 mL) and 2 mL of each colloidal solution (1 μmol metal). After sealing, the reactor was purged with $95\%CH_4–5\%N_2$ (3 MPa) three times to remove residual air. Then, the autoclave was re-pressurized to 3 MPa and heated to the desired temperature at a rate of 2 °C min^{-1}. When the reaction temperature reached 50 °C, stirring was started (800 rpm) and continued for 0.5 h. After reaction, the reactor was cooled in ice–water (*ca.* 10 °C) to minimize the volatility of the liquid products. The gas phase products were collected using a gas sample bag (100 mL) and analysed by gas chromatography on an Agilent 7890B gas chromatograph equipped with two columns of Porapak-Q and 5A and a thermal conductivity detector (He carrier gas) using N_2 as an internal standard. Only CO_2 was detected in the gas phase. ^{1}H-NMR (Bruker, 400 MHz) spectroscopy was used to determine and quantify the liquid phase products. Water suppression was employed to minimise the signal arising from water. Typically, 0.2 mL D_2O, 1.0 mL sample and DMSO as an internal standard were placed in a NMR tube. ^{1}H-NMR spectra were recorded with a recycle delay of 5 s and a spinning rate of 64 scans. The methanol selectivity and productivity were estimated using the following equations:[53,54]

$$\text{Primary oxygenate selectivity} = \text{mole of } (CH_3OH + CH_3OOH)/\text{total mole of products.}$$

$$\text{Primary oxygenate productivity} = \text{mole of } (CH_3OH + CH_3OOH)/(\text{weight of metal (kg)} \times \text{reaction time (h)})$$

2.3 Catalyst characterization

To determine the morphology and size of the Pd@Pt NPs, transmission electron microscopy (TEM) measurements were performed. For that purpose, the materials were dispersed on a 300-mesh copper TEM grid covered with a carbon film. Low and high resolution transmission electron microscopy (TEM and HRTEM) observations were carried out with a JEOL JEM-ARM200F Cold FEG (cold field emission gun) equipped with a probe corrector and coupled to an EDX spectrometer and an electron energy loss spectrometer (EELS). The size distribution was acquired by measuring a minimum of 300 objects and was given as mean standard deviation according to a Gaussian fit of the corresponding size distribution.

CO adsorption-*in situ* diffuse reflectance infrared Fourier transform spectroscopy (DRIFTS) studies were performed using a Thermo Nicolet iS50-FT-IR spectrometer equipped with a gas-dosing system and a ZnSe window. The IR spectra were recorded at atmospheric pressure with 4 cm^{-1} in absorbance mode and a resolution of 64 scans. The colloidal suspensions (containing *ca.* 5 mg of NPs) were dried in a freeze dryer for 48 h before their transfer into an *in situ* FT-IR chamber. A nitrogen (x) flux with a flow rate of 50 mL min^{-1} was applied to clean the catalyst surface before measurement. Then 5 vol% CO/N_2 gas was introduced into the FT-IR chamber for 30 min at r.t. in order to reach a saturated coverage. The CO adsorption-IR spectra were obtained after the signal for physisorbed CO species disappeared.

The chemical state and the surface composition of the catalysts were analyzed by X-ray photoelectron spectroscopy (XPS) on an XSAM 800 spectrometer (Kratos Co., Ltd.) utilizing Mg Kα radiation operating at a power of 150 W. The colloidal samples were previously dried in a freeze dryer for 48 h. XPS analysis was carried out at 13 kV and 20 mA with a sweep time of 60 s. Pass energies of 160 eV and 40 eV were employed to measure the wide scan and high resolution spectra with a step size of 1.0 eV and 0.1 eV, respectively. The signal was corrected using the C1s peak level at 284.6 eV. The XPS spectra were fitted using a Gaussian–Lorentzian function with a Shirley background using Casa XPS software.

WAXS analysis. To investigate the average structure of the NPs, wide-angle X-ray scattering (WAXS) studies were performed.[59] The powder was sealed in a Lindemann glass capillary of 1 mm in diameter. Measurements were carried out using a diffractometer dedicated to the study of amorphous and nanocrystalline samples equipped with a Mo radiation source (0.71069 nm) and a solid state detector in order to achieve low background and effective rejection of X-ray fluorescence radiation. Typical measurements covered a range of 129° in 2 theta with a collection time of 64 h. To access the radial distribution function (RDF), data were reduced and then Fourier transformed using classic procedures.

3. Results and discussion

Metal NPs were synthesized by a classical wet chemistry method using $NaBH_4$ as a reductant, PVP as a stabilizer and water as a solvent. The resulting colloidal aqueous suspensions were directly evaluated in methane oxidation using H_2O_2 as an oxidant at 3 MPa pressure and 50 °C. Initially, the catalytic activity of monometallic Pd, monometallic Pt, and bimetallic Pd_xPt_y (x/y = 1/8, 1/4, 1/2, 1/1, 2/1, 4/1, 8/1) colloidal catalysts was investigated. A representative NMR spectrum is shown in Fig. 1, where the peaks corresponding to CH_3OH (δ = 3.2), CH_3OOH (δ = 3.7), HCHO (δ = 4.8), HCOOH (δ = 8.1), and dissolved CH_4 (δ = 0.0) were clearly identified. The results of catalytic data are summarized in Table 1. The two metal chloride precursors, their mixture (Table 1, entries 10–12) and PVP alone (Table S1†) displayed no catalytic activity for CH_4 oxidation, suggesting that the metal NPs were the active species. No carbon-containing products were found in the liquid phase or gas phase when CH_4 was not charged into the reactor (Table S1†), ruling out the possibility of PVP conversion into C_1 organic products.

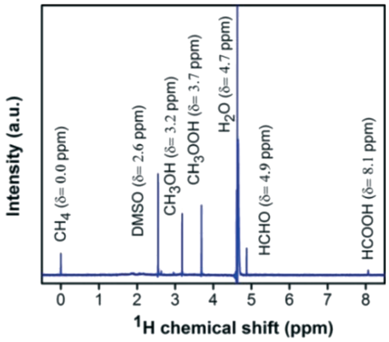

Fig. 1 Representative ^1H-NMR spectrum resulting from CH_4 oxidation experiments with identification of the formed products.

As shown in Table 1, methanol was the only product detected in the liquid phase using the monometallic Pt NP catalyst (entry 1). A small amount of CO_2 (6%) was also generated. Despite the high selectivity (94%), the productivity was relatively low (3.0 mol mol_{metal}^{-1} h^{-1}). With the monometallic Pd NP catalyst (entry 9), formaldehyde was formed, leading to a reduced selectivity to methanol (80%). On the other hand, the productivity of methanol increased to 7.8 mol mol_{metal}^{-1} h^{-1}, suggesting excellent methane activation ability over Pd NPs. Concerning the series of bimetallic Pt_xPd_y NPs, interestingly, reducing the ratio of Pt to Pd (entries 5–8) resulted in a decrease in the methanol selectivity but an increase in the productivity. For instance, the bimetallic Pt_1Pd_1 NP catalyst exhibited a high selectivity (86%) and yield (9.4 mol mol_{metal}^{-1} h^{-1}), exhibiting superior productivity towards C_1 primary oxygenates to that obtained over the monometallic Pt NPs and Pd NPs. To identify the most suitable configuration of Pd and Pt in the PdPt bimetallic NPs for methane oxidation, Pt@Pd and Pd@Pt NPs were prepared following a seeded growth method and further tested (entries 13 and 14). Pt@Pd NPs present better productivity and worse selectivity than Pt_1Pd_1 does, which is ascribed to the higher activity but worse methanol selectivity of exposed Pd. Pd@Pt NPs, on the other hand, provided a higher selectivity (92%) and productivity (13.4 mol mol_{metal}^{-1} h^{-1}, 89.3 mol $kg_{catalyst}^{-1}$ h^{-1}) toward methanol than alloy PtPd NPs. Note that Pd@Pt NPs are significantly better in productivity than Pt enriched Pt_xPd_y NPs which have similar surface structures, demonstrating the unique properties of Pd@Pt prepared by consecutive reduction. The performance

Table 1 Catalytic performance of the NP samples and metal precursors tested for direct methane oxidation[a]

		Concentration of product (mol mol_{metal}^{-1})						
Entry	Catalysts: Pt_xPd_y	CH_3OH	CH_3OOH	HCHO	HCOOH	CO_2	Primary oxygenate selectivity (%)	Primary oxygenate productivity (mol mol_{metal}^{-1} h^{-1})
1	x/y = 10/0	1.5	0	0	0	0.1	94	3.0
2	x/y = 8/1	2.0	0	0	0	0.1	95	4.0
3	x/y = 4/1	2.7	0	0	0	0.2	93	5.4
4	x/y = 2/1	3.2	0	0	0	0.3	91	6.4
5	x/y = 1/1	3.5	1.2	0.4	0	0.4	86	9.4
6	x/y = 1/2	3.7	2.6	0.9	0.7	0.4	76	12.6
7	x/y = 1/4	2.8	3.7	4.4	3.1	0.4	45	13.0
8	x/y = 1/8	3.0	3.6	1.6	0.4	0.5	72	13.2
9	x/y = 0/10	2.4	1.5	0.6	0	0.4	80	7.8
10	K_2PtCl_4	0	0	0	0	0.3	0	0
11	H_2PdCl_4	0	0	0	0	0.5	0	0
12	K_2PtCl_4 + H_2PdCl_4	0	0	0	0	0.4	0	0
13	Pt@Pd	2.8	3.4	0.8	1.0	0.5	73	12.4
14	Pd@Pt	2.3	4.4	0.3	0	0.3	92	13.4

[a] Catalysis conditions: 1 μmol metal in 2 mL deionized water, 30 bar CH_4, 0.4 mL of 1 M H_2O_2, 50 °C for 0.5 h, 800 rpm.

obtained with the Pd@Pt catalyst is comparable to or even better than that of recently published systems like Au–Pd colloids,[52] AuPd/ZSM-5-R,[54] PdxCu1−xO/C (ref. 60) and Rh/TiO_2 (ref. 43) (Table S3†). The gain factor of Pd@Pt was determined by measuring the consumption of H_2O_2 (Table S4†). The H_2O_2 utilization efficiency of Pd@Pt is also comparable to that of reported Au–Pd systems.[53] The system is scalable when the reaction volume is increased four times, although the primary oxygenate productivity is lower probably because of mass transfer limitation (Table S5†).

TEM analysis revealed the presence of isolated Pd@Pt NPs together with aggregates of 10–50 nm in size (Fig. S1†). An average size of 3.4 ± 2.2 nm was determined for the Pd@Pt NPs. STEM-EDX analysis on the NP aggregates indicated close mass contents of Pd and Pt (*ca.* 54 and 46%, respectively; Fig. S2†). Few isolated pure Pt NPs (Fig. S3†) were also observed. Given their mean size, the calculated turnover frequency (TOF) per surface metal site of Pd@Pt NPs was found to be 34.0 h^{-1} (Fig. S4 and Table S2†). This result is much higher than those of the Pd, Pt or PdPt samples, indicating a different intrinsic activity.

Fig. 2 presents the STEM-EDX analysis of the Pd@Pt NPs. The elemental mapping clearly evidenced a predominant enrichment of Pd in the NP core while the surface layer is more Pt-enriched, thus indicating NPs with a Pd-core–Pt-shell structure. The Fourier transform of a STEM-HRTEM dark field image of Pd@Pt particles showed only one diffraction pattern attributable to Pt. This result indicates potential epitaxial growth of Pt over Pd cores (Fig. S5†). The analysis above suggests that the sample comprises both core–shell Pd@Pt NPs and pure Pt NPs. Compared with the activity data of Pt NPs (entry 1, Table 1), the Pd@Pt sample (entry 14) showed significantly enhanced oxygenate productivity, supporting the dominant role of the core–shell structure in providing superior activity.

In order to complete the structural analysis of the Pd@Pt NPs, WAXS analysis was applied. As shown in Fig. S6,† the diffractogram obtained corresponds well to the fcc structure, just like Pd and Pt, however much better agreement with pure Pd can be observed. The related crystallographic parameter was estimated to be 0.3898 nm, intermediate between values for pure Pd (0.3890 nm) and pure Pt (0.3923 nm). For bimetallic NPs, deviation to Vegard's law was previously observed and related to core–shell organization rather than alloying.[59] In the present case, the minimal deviation to the Pd parameter points to segregation with Pd at the core and Pt at the shell. Regarding Pt, the structural order remains ambiguous since as a rule the thin less

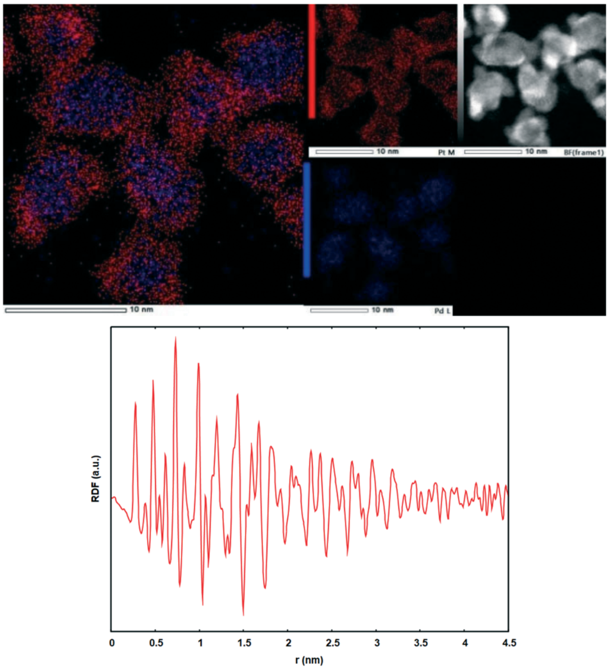

Fig. 2 Top: STEM-EDX elemental mapping of Pd@Pt NPs where platinum appears in red and palladium in blue. Bottom: Radial distribution function (RDF) of the Pd@Pt NP sample.

ordered shell marginally contributes to the scattering and WAXS alone cannot distinguish between a disordered shell and a well ordered one in epitaxial growth over a Pd core. In real space (Fig. 2), the lack of short C–C distances confirms that PVP contribution to scattering can be neglected. On the basis of coherence length, the average size for crystallites is in the range of 3.6–3.9 nm.

XPS analysis was performed on the Pd@Pt nanocatalyst (Fig. S7†). 59% of surface Pt is Pt^0 (Pt_{4f} ~ 70.8 eV)[61] and 39% of surface Pd is Pd^0 (Pd_{3d} ~ 335.0 eV),[62,63] likely due to oxidation of both elements after synthesis. CO adsorption experiments were carried out on the Pd, Pt and Pd@Pt catalysts using the DRIFTS technique (Fig. 3). The IR bands observed at 1972 and 1913 cm^{-1} for Pd–PVP NPs can be assigned to the bridging CO adsorption on the step sites of Pd NPs or on the Pd(100)/Pd(111) facets.[64–66] The predominant 2130 cm^{-1} IR peak corresponds to the linear Pd^{2+}–CO bond,[62,67,68] thus suggesting partial oxidation of metallic Pd during the sample preparation, which is consistent with the XPS results. For Pt NPs, only one CO absorption band is visible at 2056 cm^{-1}, which is ascribed to linearly adsorbed CO on unsaturated Pt sites.[69,70] A similar phenomenon was observed with Pd@Pt NPs, thus confirming that Pt is located at the NP surface. However, on Pd@Pt NPs the CO absorption band appears at a lower wavenumber than that observed on Pt NPs (2051 cm^{-1} against 2056 cm^{-1}). This shift towards lower frequencies is ascribed to an electron transfer from Pd to Pt due to their electronegativity difference.

The Pd@Pt NP catalyst was further investigated. Fig. 4a shows its catalytic performances obtained at 25, 50, and 70 °C, respectively. Pd@Pt NPs provided a much lower productivity (oxygenate product: 2.2 μmol) despite a high methanol selectivity (89%) at 25 °C. Increasing the temperature to 70 °C significantly enhanced the yield (oxygenate products: 8.2 μmol) but slightly decreased the methanol selectivity (87%) due to the favorable formation of CO_2 as a by-product. Interestingly, the reaction performed at 50 °C evidenced considerably improved catalytic activity (oxygenate products: 7.0 μmol) and selectivity (92.4%). From the slope of the Arrhenius plot, the apparent activation energy is estimated to be 45 kJ mol^{-1}, a value that is comparable to those previously reported with highly active catalysts.[33,52,53] To confirm the high selectivity towards C1 primary oxygenate products observed with the Pd@Pt colloidal catalyst, methanol was used as the reactant instead of methane (Fig. 4b). Only a low conversion (*ca.* 10%) of methanol into formaldehyde was observed under these conditions, suggesting that Pd@Pt NPs are not active for the oxidation of methanol, thus minimizing undesired over-oxidation.

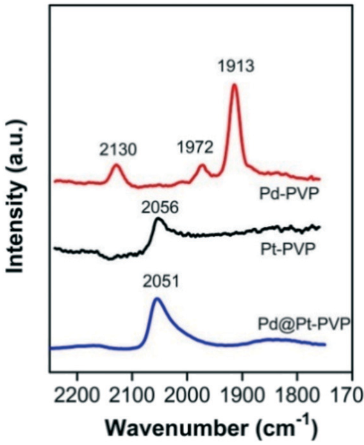

Fig. 3 *In situ* DRIFTS spectra of CO chemisorption on Pd, Pt and Pd@Pt NP samples at r.t.

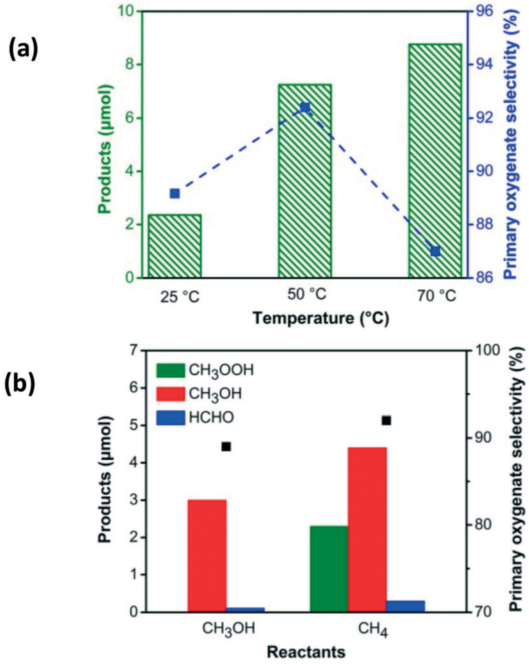

Fig. 4 (a) Activity and selectivity obtained in methane oxidation at 25, 50, and 70 °C with 400 μmol of H_2O_2 and 30 bar CH_4 over Pd@Pt NPs; (b) catalytic performance using CH_3OH (3.2 μmol) and CH_4 (30 bar) as reactants over Pd@Pt NPs.

Kinetic analysis was performed by changing the H_2O_2 concentration and CH_4 pressure. As shown in Fig. 5a–c, the reaction is first order with regard to both H_2O_2 and CH_4 under the tested conditions ($[H_2O_2]$ = 100–400 μmol, $P(CH_4)$ = 10–30 bar). The rate-determining step, therefore, involves both activation of H_2O_2 and CH_4. On the basis of H_2O_2 consumption, the initial rate was employed to calculate the pseudo first-order rate constant at the applied temperature.

Fig. 5d presents the variation of catalytic performance of CH_4 oxidation as a function of H_2O_2 concentration. The Pd@Pt NP catalyst showed a volcano-shaped dependence of the oxygenated products on the amount of H_2O_2 added. A similar trend was also observed on the selectivity to methanol. Increasing the H_2O_2 amount from 400 to 4000 μmol led to a remarkable, monotonous decrease in both oxygenated products (from 7 to 1.2 μmol) and methanol selectivity (from 92% to 42%). According to the literature,[16,49]

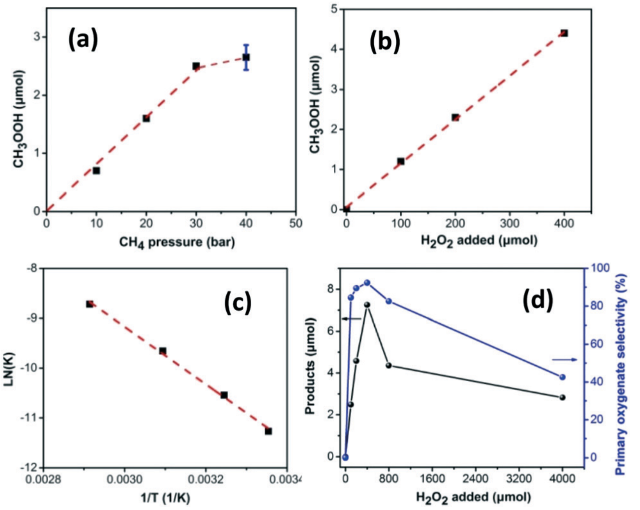

Fig. 5 Dependence of the amount of formed CH_3OOH on (a) CH_4 pressure and (b) concentration of H_2O_2 added; (c) the Arrhenius plot for the methane oxidation reaction; (d) effects of H_2O_2 concentration on the productivity and selectivity over Pd@Pt NPs at 50 °C for 0.5 h.

H_2O_2 undergoes splitting supplying $^{\bullet}OH$ radicals, and the activation of CH_4 occurred *via* a radical mechanism. It was reported that excess H_2O_2 leads to termination of the reaction and thus reduces the product formation.[53] Note that the Pd@Pt NP catalyst precipitated to some extent in the presence of a large amount of H_2O_2 (4000 μmol) (Fig. S8†). Decreasing the H_2O_2 concentration from 400 to 100 μmol led to a decline in both C1 liquid products (from 7 to 2.4 μmol) and methanol selectivity (from 92% to 84%). This may be due to the limited amount of available radicals in the reaction mixture. There is thus an optimum H_2O_2 concentration to achieve the highest methanol selectivity and yield.

The reaction pathway was studied by analyzing the evolution of the products as a function of time (up to 170 min, Fig. 6). The amount of CH_3OOH increased progressively in the first 80 min and decreased afterwards. However, the quantity of CH_3OH, HCHO, HCOOH, and CO_2 continued to increase with the reaction time. In addition, CH_3OOH and CH_3OH appeared in the product stream from the beginning, while HCHO and CO_2 were only observed after 30 min. The total yield of products firstly showed an upsurge and then, decreased from 80 min onwards. This is in agreement with the consumption rate of H_2O_2 in the reaction medium (Table S6†). Extra H_2O_2 was added into the reaction mixture after 80 min. A similar oxidation rate was attained and thus more oxygenate products were formed. Besides, no obvious precipitation for the Pd@Pt NP catalyst was observed at the end of the reaction.

These results indicate that CH_4 was first converted into CH_3OOH, which may be formed *via* the reaction between $^{\bullet}CH_3$ and $^{\bullet}OOH$, or between $CH_3OO^{\bullet}$ and $^{\bullet}H$.[33,53] It was previously well established that CH_3OOH can be easily deoxidized to CH_3OH.[16,41,53] Further oxidation of CH_3OH can lead to HCHO, HCOOH, and CO_2.[48,49] Here, when CH_3OH was directly used as the reactant instead of CH_4 (Fig. 4b), formation of a small amount of HCHO and CO_2 was confirmed by ^1H NMR and GC-TCD analysis, respectively. Combined, CH_3OOH is a key intermediate in the reaction, which is formed *via* CH_4 oxidation and is then converted into CH_3OH, HCHO, HCOOH, and CO_2.[35,41,48,49,53]

A three step reaction mechanism is proposed in Scheme 1. In step 1, the decomposition of H_2O_2 catalyzed by Pd@Pt produces H_2O and O_2 as well as three radicals $^{\bullet}H$, $^{\bullet}OOH$, and $^{\bullet}OH$. Compared with $^{\bullet}H$ and $^{\bullet}OOH$, the $^{\bullet}OH$ radical species is known to be highly effective for methane activation *via* subtraction of a H atom to produce $^{\bullet}CH_3$ radicals (step (2)).[16,22,36] An Fe-based Fenton type catalyst, well-known for its ability to generate $^{\bullet}OH$ radicals,[71,72] was also investigated (Table S7†). A significantly lower amount of products was detected over this Fe-based Fenton type catalyst compared with that over Pd@Pt NPs, demonstrating that the Pd@Pt nanocatalyst also played an active role in methane activation in step (2). Considering the first order kinetic behavior, we propose that both H_2O_2 and methane are adsorbed on the surface of NPs with comparable coverage. H_2O_2 dissociates to provide $^{\bullet}OH$ radicals at the surface of Pd@Pt NPs, which then activate adsorbed CH_4 by forming $^{\bullet}CH_3$ radicals. In the solution, $^{\bullet}OH$ is able to oxidize H_2O_2 to form more stable $^{\bullet}OOH$ species,[73] so that in the liquid phase

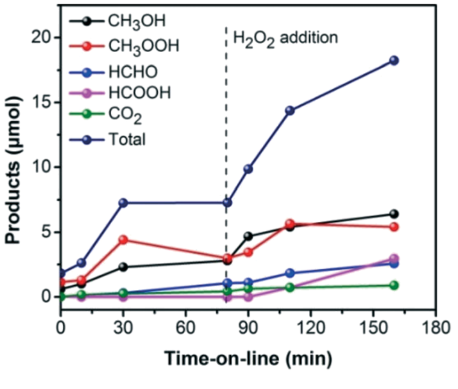

Fig. 6 Catalytic performance of CH_4 oxidation over Pd@Pt NPs with various reaction times and reusability investigation.

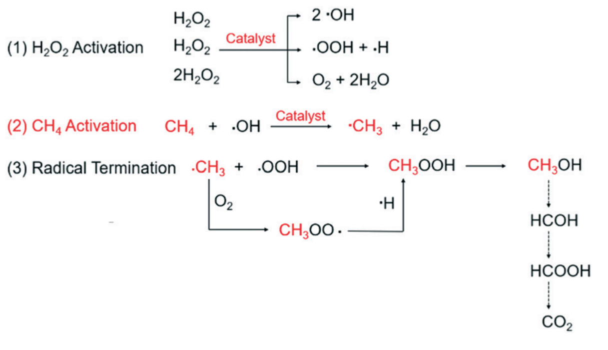

Scheme 1 Schematic representation of the proposed radical mechanism.

$^{\bullet}$OOH would be dominant. As such, selective oxidation of methane mainly occurs on the catalyst surface rather than in the solution. As far as we are aware, the active role of surface reactions on NPs in H_2O_2 oxidized methane conversion to methanol has not been explicitly mentioned in previous studies.

Conclusions

In this work, core–shell Pd@Pt NPs proved to be a performant catalyst for methanol synthesis *via* the direct oxidation of methane in water using H_2O_2 as an oxidant and mild reaction conditions. This catalyst led to a high selectivity (92.4%) and productivity (89.3 mol $\text{kg}_{\text{catalyst}}^{-1}$ h^{-1}) and was found stable with time-on-line testing at 50 °C and 167 mM H_2O_2. A consecutive oxidation pathway *via* a radical mechanism was identified: methane was firstly converted to methyl hydroperoxide and methanol, and methanol was then oxidized to formaldehyde, formic acid, and carbon dioxide. As evidenced from the control experiments and kinetic analysis, Pd@Pt NPs were crucial for the activation of methane, and played a positive role in both H_2O_2 splitting and C–H bond activation. *In situ* CO-DRIFTS results indicated a high surface electron density around Pt due to Pd electron donation, and this electronic interaction between Pt and Pd may be the origin of the enhanced catalytic performance.

Conflicts of interest

There are no conflicts to declare.

Acknowledgements

The French National Agency for Research (project no ANR-17-CE06-0017-01) and the Singapore National Research Foundation (WBS: R-279-000-530-281) are gratefully acknowledged for the financial support. The authors also thank the UMS R. Castaing Microcharacterization Center for the access to electron microscopy equipment.

References

1 R. A. Kerr, *Science*, 2010, **328**, 1624–1626.
2 B. Liu, L. Tian, L. Li, C. Au and A. C. Cheung, *AIChE J.*, 2011, **57**, 1852–1859.
3 C. D. Elvidge, M. Zhizhin, K. Baugh, F.-C. Hsu and T. Ghosh, *Energies*, 2016, **9**, 14.
4 E. McFarland, *Science*, 2012, **338**, 340–342.
5 M. Kumar, G. Rattan and R. Prasad, *Can. Chem. Trans.*, 2015, **3**, 381–409.
6 P. Tang, Q. Zhu, Z. Wu and D. Ma, *Energy Environ. Sci.*, 2014, **7**, 2580–2591.
7 T. V. Choudhary and V. R. Choudhary, *Angew. Chem., Int. Ed.*, 2008, **47**, 1828–1847.
8 J. R. Rostrup-Nielsen, J. Sehested and J. K. Nørskov, *Adv. Catal.*, 2002, **47**, 65–139.
9 S. Bharadwaj and L. Schmidt, *Fuel Process. Technol.*, 1995, **42**, 109–127.
10 M. E. Dry, *Catal. Today*, 2002, **71**, 227–241.
11 J. R. Rostrup-Nielsen, *Catal. Today*, 1993, **18**, 305–324.
12 I. Dybkjær and K. Aasberg-Petersen, *Can. J. Chem. Eng.*, 2016, **94**, 607–612.
13 A. Caballero and P. J. Pérez, *Chem. Soc. Rev.*, 2013, **42**, 8809–8820.
14 E. Fiedler, G. Grossmann, D. B. Kersebohm, G. Weiss and C. Witte, *Ullmann's encyclopedia of industrial chemistry*, 2000.
15 M. Behrens, F. Studt, I. Kasatkin, S. Kühl, M. Hävecker, F. Abild-Pedersen, S. Zander, F. Girgsdies, P. Kurr and B.-L. Kniep, *Science*, 2012, **336**, 893–897.
16 A. I. Olivos-Suarez, À. Szécsényi, E. J. M. Hensen, J. Ruiz-Martinez, E. A. Pidko and J. Gascon, *ACS Catal.*, 2016, **6**, 2965–2981.
17 B. A. Arndtsen, R. G. Bergman, T. A. Mobley and T. H. Peterson, *Acc. Chem. Res.*, 1995, **28**, 154–162.
18 A. Holmen, *Catal. Today*, 2009, **142**, 2–8.
19 X. Guo, G. Fang, G. Li, H. Ma, H. Fan, L. Yu, C. Ma, X. Wu, D. Deng, M. Wei, D. Tan, R. Si, S. Zhang, J. Li, L. Sun, Z. Tang, X. Pan and X. Bao, *Science*, 2014, **344**, 616–619.
20 R. Horn and R. Schlögl, *Catal. Lett.*, 2015, **145**, 23–39.
21 A. Galadima and O. Muraza, *J. Ind. Eng. Chem.*, 2016, **37**, 1–13.
22 P. Schwach, X. Pan and X. Bao, *Chem. Rev.*, 2017, **117**, 8497–8520.
23 Y. Dou, Y. Pang, L. Gu, Y. Ding, W. Jiang, X. Feng, W. Ji and C.-T. Au, *J. Energy Chem.*, 2018, **27**, 883–889.
24 C.-G. Zhan, J. A. Nichols and D. A. Dixon, *J. Phys. Chem. A*, 2003, **107**, 4184–4195.
25 M. C. Paganini, M. Chiesa, P. Martino, E. Giamello and E. Garrone, *J. Phys. Chem. B*, 2003, **107**, 2575–2580.
26 R. A. Periana, D. J. Taube, S. Gamble, H. Taube, T. Satoh and H. Fujii, *Science*, 1998, **280**, 560–564.
27 M. O. Adebajo, *Green Chem.*, 2007, **9**, 526–539.
28 M. Ahlquist, R. J. Nielsen, R. A. Periana and W. A. Goddard III, *J. Am. Chem. Soc.*, 2009, **131**, 17110–17115.
29 K. Otsuka and Y. Wang, *Appl. Catal., A*, 2001, **222**, 145–161.
30 A. A. Latimer, A. Kakekhani, A. R. Kulkarni and J. K. Nørskov, *ACS Catal.*, 2018, **8**, 6894–6907.
31 E. G. Chepaikin, G. N. Boyko, A. P. Bezruchenko, A. A. Leshcheva and E. H. Grigoryan, *J. Mol. Catal. A: Chem.*, 1998, **129**, 15–18.
32 R. A. Periana, D. J. Taube, E. R. Evitt, D. G. Löffler, P. R. Wentrcek, G. Voss and T. Masuda, *Science*, 1993, **259**, 340–343.
33 C. Hammond, M. M. Forde, M. H. Ab Rahim, A. Thetford, Q. He, R. L. Jenkins, N. Dimitratos, J. A. Lopez-Sanchez, N. F. Dummer, D. M. Murphy, A. F. Carley, S. H. Taylor, D. J. Willock, E. E. Stangland, J. Kang, H. Hagen, C. J. Kiely and G. J. Hutchings, *Angew. Chem., Int. Ed.*, 2012, **51**, 5129–5133.
34 M. H. Ab Rahim, M. M. Forde, R. L. Jenkins, C. Hammond, Q. He, N. Dimitratos, J. A. Lopez-Sanchez, A. F. Carley, S. H. Taylor, D. J. Willock, D. M. Murphy, C. J. Kiely and G. J. Hutchings, *Angew. Chem., Int. Ed.*, 2013, **52**, 1280–1284.

35 S. Al-Shihri, C. J. Richard and D. Chadwick, *ChemCatChem*, 2017, **9**, 1276–1283.

36 P. Tomkins, M. Ranocchiari and J. A. van Bokhoven, *Acc. Chem. Res.*, 2017, **50**, 418–425.

37 M. H. Mahyuddin, A. Staykov, Y. Shiota and K. Yoshizawa, *ACS Catal.*, 2016, **6**, 8321–8331.

38 M. Ravi, M. Ranocchiari and J. A. van Bokhoven, *Angew. Chem., Int. Ed.*, 2017, **56**, 16464–16483.

39 D. P. Vitaly, L. Sushkevich, M. Ranocchiari and J. A. van Bokhoven, *Science*, 2017, **356**, 523–527.

40 Y. K. Chow, N. F. Dummer, J. H. Carter, C. Williams, G. Shaw, D. J. Willock, S. H. Taylor, S. Yacob, R. J. Meyer, M. M. Bhasin and G. J. Hutchings, *Catal. Sci. Technol.*, 2018, **8**, 154–163.

41 X. Meng, X. Cui, N. P. Rajan, L. Yu, D. Deng and X. Bao, *Chem*, 2019, **5**, 2296–2325.

42 Y. Kwon, T. Y. Kim, G. Kwon, J. Yi and H. Lee, *J. Am. Chem. Soc.*, 2017, **139**, 17694–17699.

43 J. Shan, M. Li, L. F. Allard, S. Lee and M. Flytzani-Stephanopoulos, *Nature*, 2017, **551**, 605–608.

44 S. Bai, F. Liu, B. Huang, F. Li, H. Lin, T. Wu, M. Sun, J. Wu, Q. Shao, Y. Xu and X. Huang, *Nat. Commun.*, 2020, **11**, 954.

45 Y. L. Yu Tang, V. Fung, D. Jiang, W. Huang, S. Zhang, Y. Iwasawa, L. N. Tomohiro Sakata, X. Zhang, A. I. Frenkel and F. Tao, *Nat. Commun.*, 2018, **9**, 1231.

46 A. Wang, J. Li and T. Zhang, *Nat. Rev. Chem.*, 2018, **2**, 65–81.

47 W. Huang, S. Zhang, Y. Tang, Y. Li, L. Nguyen, Y. Li, J. Shan, D. Xiao, R. Gagne, A. I. Frenkel and F. Tao, *Angew. Chem., Int. Ed.*, 2016, **55**, 13441–13445.

48 X. Cui, H. Li, Y. Wang, Y. Hu, L. Hua, H. Li, X. Han, Q. Liu, F. Yang, L. He, X. Chen, Q. Li, J. Xiao, D. Deng and X. Bao, *Chem*, 2018, **4**, 1902–1910.

49 Q. Shen, C. Cao, R. Huang, L. Zhu, X. Zhou, Q. Zhang, L. Gu and W. Song, *Angew. Chem.*, 2020, **132**, 1232–1235.

50 R. J. Lewis, A. Bara-Estaun, N. Agarwal, S. J. Freakley, D. J. Morgan and G. J. Hutchings, *Catal. Lett.*, 2019, **149**, 3066–3075.

51 Y. He, C. Luan, Y. Fang, X. Feng, X. Peng, G. Yang and N. Tsubaki, *Catal. Today*, 2020, **339**, 48–53.

52 R. McVicker, N. Agarwal, S. J. Freakley, Q. He, S. Althahban, S. H. Taylor, C. J. Kiely and G. J. Hutchings, *Catal. Today*, 2020, **342**, 32–38.

53 N. Agarwal, S. J. Freakley, R. U. McVicker, S. M. Althahban, N. Dimitratos, Q. He, D. J. Morgan, R. L. Jenkins, D. J. Willock, S. H. Taylor, C. J. Kiely and G. J. Hutchings, *Science*, 2017, **358**, 223–227.

54 Z. Jin, L. Wang, E. Zuidema, K. Mondal, M. Zhang, J. Zhang, C. Wang, X. Meng, H. Yang, C. Mesters and F.-S. Xiao, *Science*, 2020, **367**, 193–197.

55 Q. Zhao, B. Liu, Y. Xu, F. Jiang and X. Liu, *New J. Chem.*, 2020, **44**, 1632–1639.

56 U. Achatz, C. Berg, S. Joos, B. S. Fox, M. K. Beyer, G. Niedner-Schatteburg and V. E. Bondybey, *Chem. Phys. Lett.*, 2000, **320**, 53–58.

57 G. Psofogiannakis, A. St-Amant and M. Ternan, *J. Phys. Chem. B*, 2006, **110**, 24593–24605.

58 L. Xiao and L. Wang, *J. Phys. Chem. B*, 2007, **111**, 1657–1663.

59 C. Bergounhou, C. Blandy, R. Choukroun, P. Lecante, C. Lorber and J.-L. Pellegatta, *New J. Chem.*, 2007, **31**, 218–223.

60 S. Bai, Y. Xu, P. Wang, Q. Shao and X. Huang, *ACS Catal.*, 2019, **9**, 6938–6944.

61 J. Chen, Y. Wu, W. Hu, P. Qu, X. Liu, R. Yuan, L. Zhong and Y. Chen, *Mol. Catal.*, 2020, **496**, 111185.

62 J. Chen, J. Zhong, Y. Wu, W. Hu, P. Qu, X. Xiao, G. Zhang, X. Liu, Y. Jiao, L. Zhong and Y. Chen, *ACS Catal.*, 2020, **10**, 10339–10349.

63 J. Chen, Y. Wu, W. Hu, P. Qu, G. Zhang, P. Granger, L. Zhong and Y. Chen, *Appl. Catal., B*, 2020, **264**, 118475.

64 J. H. Carter, S. Althahban, E. Nowicka, S. J. Freakley, D. J. Morgan, P. M. Shah, S. Golunski, C. J. Kiely and G. J. Hutchings, *ACS Catal.*, 2016, **6**, 6623–6633.

65 L. Ding, H. Yi, W. Zhang, R. You, T. Cao, J. Yang, J. Lu and W. Huang, *ACS Catal.*, 2016, **6**, 3700–3707.

66 K. Murata, Y. Mahara, J. Ohyama, Y. Yamamoto, S. Arai and A. Satsuma, *Angew. Chem.*, 2017, **129**, 1–6.

67 Y. Lou, J. Ma, W. Hu, Q. Dai, L. Wang, W. Zhan, Y. Guo, X.-M. Cao, Y. Guo, P. Hu and G. Lu, *ACS Catal.*, 2016, **6**, 8127–8139.

68 S. Royer and D. Duprez, *ChemCatChem*, 2011, **3**, 24–65.

69 Q. Sun, N. Wang, Q. Fan, L. Zeng, A. Mayoral, S. Miao, R. Yang, Z. Jiang, W. Zhou, J. Zhang, T. Zhang, J. Xu, P. Zhang, J. Cheng, D.-C. Yang, R. Jia, L. Li, Q. Zhang, Y. Wang, O. Terasaki and J. Yu, *Angew. Chem., Int. Ed.*, 2020, **132**, 19618–19627.

70 J. Zhu, T. Wang, X. Xu, P. Xiao and J. Li, *Appl. Catal., B*, 2013, **130–131**, 197–217.

71 F. Haber, J. Weiss and W. J. Pope, *Proc. R. Soc. London, Ser. A*, 1934, **147**, 332–351.

72 A. Babuponnusami and K. Muthukumar, *J. Environ. Chem. Eng.*, 2014, **2**, 557–572.

73 R. J. Buszek, M. Torrent-Sucarrat, J. M. Anglada and J. S. Francisco, *J. Phys. Chem. A*, 2012, **116**, 5821–5829.